Response of a CMS HGCAL silicon-pad electromagnetic calorimeter prototype to 20-300 GeV positrons

CMS HGCAL collaboration

B. Acar,[2] G. Adamov,[13] C. Adloff,[37] S. Afanasiev,[26] N. Akchurin,[45] B. Akgün,[2] F. Alam Khan,[4] M. Alhusseini,[25] J. Alison,[5] A. Alpana,[19] G. Altopp,[3] M. Alyari,[8] S. An,[5] S. Anagul,[6] I. Andreev,[24] P. Aspell,[4] I. O. Atakisi,[2] O. Bach,[7] A. Baden,[30] G. Bakas,[38] A. Bakshi,[8] P. Bargassa,[27] D. Barney,[4] F. Beaudette,[28] F. Beaujean,[28] E. Becheva,[28] A. Becker,[4] P. Behera,[20] A. Belloni,[30] T. Bergauer,[15] M. Besancon,[42] S. Bhattacharya,[35,43] D. Bhowmik,[43] B. Bilki,[25] P. Bloch,[21] A. Bodek,[41] M. Bonanomi,[28] A. Bonnemaison,[28] S. Bonomally,[21] J. Borg,[21] F. Bouyjou,[42] N. Bower,[11] D. Braga,[8] J. Brashear,[32] E. Brondolin,[4] P. Bryant,[5] A. Buchot Perraguin,[28] J. Bueghly,[35] B. Burkle,[3] A. Butler-Nalin,[46] O. Bychkova,[31] S. Callier,[40] D. Calvet,[42] X. Cao,[16] A. Cappati,[28] B. Caraway,[1] S. Caregari,[37] A. Cauchois,[28] L. Ceard,[39] Y. C. Cekmecelioglu,[2] S. Cerci,[22] G. Cerminara,[4] M. Chadeeva,[31] N. Charitonidis,[4] R. Chatterjee,[32] Y. M. Chen,[30] Z. Chen,[35] H. J. Cheng,[39] K. y. Cheng,[37] S. Chernichenko,[17] H. Cheung,[8] C. H. Chien,[39] S. Choudhury,[18] D. Čoko,[9] G. Collura,[46] F. Couderc,[42] M. Danilov,[31] D. Dannheim,[4] W. Daoud,[28] P. Dauncey,[21] A. David,[4] G. Davies,[21] O. Davignon,[28] E. Day,[5] P. DeBarbaro,[41] F. De Guio,[45] C. de La Taille,[40] M. De Silva,[7] P. Debbins,[25] M. M. Defranchis,[4] E. Delagnes,[42] J. M. Deltoro Berrio,[4] G. Derylo,[8] P. G. Dias de Almeida,[4] D. Diaz,[11] P. Dinaucourt,[40] J. Dittmann,[1] M. Dragicevic,[15] S. Dugad,[44] F. Dulucq,[40] I. Dumanoglu,[6] V. Dutta,[46] S. Dutta,[43] M. Dünser,[4] J. Eckdahl,[46] T. K. Edberg,[30] M. El Berni,[40] F. Elias,[29] S. C. Eno,[30] Yu. Ershov,[26] P. Everaerts,[21] S. Extier,[40] F. Fahim,[8] C. Fallon,[41] G. Fedi,[21] B. A. Fontana Santos Alves,[4] E. Frahm,[32] G. Franzoni,[4] J. Freeman,[8] T. French,[4] P. Gandhi,[8] S. Ganjour,[42] X. Gao,[12] A. Garcia-Bellido,[41] F. Gastaldi,[28] Z. Gecse,[8] Y. Geerebaert,[28] H. Gerwig,[4] O. Gevin,[42] S. Ghosh,[28] A. Gilbert,[35] W. Gilbert,[32] K. Gill,[4] C. Gingu,[8] S. Gninenko,[24] A. Golunov,[26] I. Golutvin,[26] T. Gonzalez,[46] N. Gorbounov,[26] L. Gouskos,[4] A. B. Gray,[4] Y. Gu,[16] F. Guilloux,[42] Y. Guler,[6] E. Gülmez,[2] J. Guo,[16] E. Gurpinar Guler,[6] M. Hammer,[8] H. M. Hassanshahi,[21] K. Hatakeyama,[1] A. Heering,[36] V. Hegde,[45] U. Heintz,[3] N. Hinton,[3] J. Hirschauer,[8] J. Hoff,[8] W.-S. Hou,[39] X. Hou,[16] H. Hua,[16] J. Incandela,[46] A. Irshad,[4] C. Isik,[6] S. Jain,[32] H. R. Jheng,[37] U. Joshi,[8] V. Kachanov,[17] A. Kalinin,[17] L. Kalipoliti,[28] A. Kaminskiy,[34] A. Kapoor,[16] O. Kara,[6] A. Karneyeu,[24] M. Kaya,[2] O. Kaya,[2] A. Kayis Topaksu,[6] A. Khukhunaishvili,[41] J. Kiesler,[4] M. Kilpatrick,[46] S. Kim,[11] K. Koetz,[11] T. Kolberg,[11] O. K. Köseyan,[25] A. Kristić,[9] M. Krohn,[32] K. Krüger,[7] N. Kulagin,[17] S. Kulis,[4] S. Kunori,[45] C. M. Kuo,[37] V. Kuryatkov,[45] S. Kyre,[46] Y. Lai,[30] K. Lamichhane,[45] G. Landsberg,[3] C. Lange,[4] J. Langford,[21] M. Y. Lee,[37] A. Levin,[17] A. Li,[46] B. Li,[16] J. H. Li,[39] Y. y. Li,[39] H. Liao,[16] D. Lincoln,[8] L. Linssen,[4] R. Lipton,[8] Y. Liu,[16] A. Lobanov,[14] R.-S. Lu,[39] M. Lupi,[4] I. Lysova,[24] A.-M. Magnan,[21] F. Magniette,[28] A. Mahjoub,[28] A. A. Maier,[4]

A. Malakhov,[26] S. Mallios,[4] I. Mandjavize,[42] M. Mannelli,[4] J. Mans,[32] A. Marchioro,[4]
A. Martelli,[21] G. Martinez,[11] P. Masterson,[46] B. Meng,[16] T. Mengke,[45] A. Mestvirishvili,[25]
I. Mirza,[44] S. Moccia,[4] G. B. Mohanty,[44] F. Monti,[16] I. Morrissey,[32] S. Murthy,[5] J. Musić,[9]
Y. Musienko,[36] S. Nabili,[30] A. Nagar,[46] M. Nguyen,[28] A. Nikitenko,[23] D. Noonan,[10] M. Noy,[4]
K. Nurdan,[2] C. Ochando,[28] B. Odegard,[46] N. Odell,[35] H. Okawa,[12] Y. Onel,[25] W. Ortez,[46]
J. Ozegović,[9] S. Ozkorucuklu,[22] E. Paganis,[39] D. Pagenkopf,[46] V. Palladino,[21] S. Pandey,[19]
F. Pantaleo,[4] C. Papageorgakis,[30] I. Papakrivopoulos,[38] J. Parshook,[5] N. Pastika,[1]
M. Paulini,[5] P. Paulitsch,[15] T. Peltola,[45] R. Pereira Gomes,[4] H. Perkins,[4] P. Petiot,[4]
T. Pierre-Emile,[28] F. Pitters,[15] E. Popova,[31] H. Prosper,[11] M. Prvan,[9] I. Puljak,[9] H. Qu,[4]
T. Quast,[4] R. Quinn,[32] M. Quinnan,[46] M. T. Ramos Garcia,[4] K. K. Rao,[44] K. Rapacz,[4]
L. Raux,[40] G. Reichenbach,[32] M. Reinecke,[7] M. Revering,[32] A. Roberts,[5] T. Romanteau,[28]
A. Rose,[21] M. Rovere,[4] A. Roy,[37] P. Rubinov,[8] R. Rusack,[32] V. Rusinov,[31] V. Ryjov,[4]
O. M. Sahin,[42] R. Salerno,[28] A. M. Sanchez Rodriguez,[4] R. Saradhy,[32] T. Sarkar,[37]
M. A. Sarkisla,[2] J. B. Sauvan,[28] I. Schmidt,[25] M. Schmitt,[35] E. Scott,[21] C. Seez,[21] F. Sefkow,[7]
S. Sharma,[19] I. Shein,[17] A. Shenai,[8] R. Shukla,[21,44] E. Sicking,[4] P. Sieberer,[4] P. Silva,[4]
A. E. Simsek,[6] Y. Sirois,[28] V. Smirnov,[26] U. Sozbilir,[6] E. Spencer,[3] A. Steen,[39] J. Strait,[8]
N. Strobbe,[32] J. W. Su,[39] E. Sukhov,[26] L. Sun,[16] D. Sunar Cerci,[22] C. Syal,[8] B. Tali,[6]
C. L. Tan,[41] J. Tao,[16] I. Tastan,[2] T. Tatli,[2] R. Thaus,[41] S. Tekten,[2] D. Thienpont,[40] E. Tiras,[25]
M. Titov,[42] D. Tlisov ,[24] U. G. Tok,[6] J. Troska,[4] L.-S. Tsai,[39] Z. Tsamalaidze,[13] G. Tsipolitis,[38]
A. Tsirou,[4] N. Tyurin,[17] S. Undleeb,[45] D. Urbanski,[32] V. Ustinov,[26] A. Uzunian,[17]
M. Van de Klundert,[7] J. Varela,[27] M. Velasco,[35] O. Viazlo,[11] M. Vicente Barreto Pinto,[4]
P. Vichoudis,[4] T. Virdee,[21] R. Vizinho de Oliveira,[4] J. Voelker,[3] E. Voirin,[8] M. Vojinovic,[21]
A. Wade,[11] C. Wang,[16] F. Wang,[16] X. Wang,[8] Z. Wang,[16] Z. Wang,[45] M. Wayne,[36] S. N. Webb,[21]
A. Whitbeck,[45] D. White,[46] R. Wickwire,[8] J. S. Wilson,[1] D. Winter,[4] H. y. Wu,[39] L. Wu,[16]
M. Wulansatiti Nursanto,[11] C. H Yeh,[37] R. Yohay,[11] D. Yu,[3] G. B. Yu,[42] S. S. Yu,[37] C. Yuan,[16]
F. Yumiceva,[10] I. Yusuff,[29] A. Zacharopoulou,[38] N. Zamiatin,[26] A. Zarubin,[26] S. Zenz,[21]
A. Zghiche,[28] H. Zhang,[16] J. Zhang,[11] Y. Zhang,[12] Z. Zhang[16]

[1] *Baylor University,*
  Waco 76706, TX, USA
[2] *Boğaziçi University,*
  Bebek 34342, Istanbul, Turkey
[3] *Brown University,*
  182 Hope Street, Providence 02912, RI, USA
[4] *CERN,*
  Espl. des Particules 1, 1211 Geneva 23, Switzerland
[5] *Carnegie Mellon University,*
  5000 Forbes Ave, Pittsburgh 15213, PA, USA
[6] *Çukurova University,*
  01330, Adana, Turkey
[7] *Deutsches Elektronen-Synchrotron DESY,*
  Notkestrasse 85 22607, Hamburg, Germany
[8] *Fermilab,*
  Wilson Road, Batavia 60510, IL, USA

[9] *Faculty of Electrical Engineering, Mechanical Engineering and Naval Architecture, University of Split, R. Boškovića 32, Split, Croatia*

[10] *Florida Institute of Technology, 150 W University Blvd, Melbourne 32901, FL, USA*

[11] *Florida State University, 600 W. College Ave., Tallahassee 32306, FL, USA*

[12] *Fudan University, 220 Handan Road, Yangpu, Shanghai 200433, China*

[13] *Georgian Technical University, 77 Kostava Str 0175, Tbilisi, Georgia*

[14] *The University of Hamburg, Institut für Experimentalphysik, Luruper Chaussee 149, 22761 Hamburg, Germany*

[15] *HEPHY Vienna, Nikolsdorfer Gasse 18, 1050 Wien, Vienna, Austria*

[16] *IHEP Beijing, 19 Yuquan Road, Shijing Shan, China*

[17] *IHEP Protvino, 142281, Protvino, Russia*

[18] *Indian Institute of Science, Bangalore, India*

[19] *Indian Institute of Science Education and Research, Dr. Homi Bhabha Road 411008, Pune, India*

[20] *Indian Institute of Technology, 60036 Chennai, India*

[21] *Imperial College, Prince Consort Road SW7 2AZ, London, United Kingdom*

[22] *Istanbul University, 34134 Vezneciler-Fatih, Istanbul, Turkey*

[23] *ITEP Moscow, B. Cheremushkinskaya ulitsa 25, 117 259, Moscow, Russia*

[24] *Institute for Nuclear Research of Russian Academy of Science, 60th Oct. Anniversary prospekt 7A, 117 312, Moscow, Russia*

[25] *The University of Iowa, 203 Van Allen Hall, Iowa City, 52242, Iowa, USA*

[26] *International Intergovernmental Organization Joint Institute for Nuclear Research JINR, 6 Joliot-Curie St, Dubna 141980, Moscow, Russia*

[27] *LIP, Avenida Prof. Gama Pinto, n° 2, 1649-003, Lisbon, Portugal*

[28] *Laboratoire Leprince-Ringuet CNRS/IN2P3, Route de Saclay, 91128 Ecole Polytechnique, France*

[29] *National Centre for Particle Physics, University of Malaya, Kuala Lumpur 50603, Malaysia*

[30] *The University of Maryland, College Park 20742, MD, USA*

[31] *National Research Nuclear University MEPhI, Kashirskoe Shosse 31, RU-115409, Moscow, Russia*

[32]*The University of Minnesota,*
116 Church Street SE, Minneapolis 55405, MN, USA

[33]*Byelorussian State University,*
240040, Minsk, Belarus

[34]*M.V. Lomonosov Moscow State University (MSU Moscow),*
1/2, Leninskie gory 119 991, Moscow, Russia

[35]*Northwestern University,*
2145 Sheridan Rd, Evanston 60208, IL, USA

[36]*University of Notre Dame,*
Notre Dame 46556, IN, USA

[37]*National Central University Taipei (NCU),*
No.300, Jhongda Rd 32001, Jhongli City, Taiwan

[38]*National Technical University of Athens,*
9, Heroon Polytechneiou Street 15780, Athens, Greece

[39]*National Taiwan University,*
10617, Taipei, Taiwan

[40]*Laboratoire OMEGA CNRS/IN2P3,*
Route de Saclay 91128, Ecole Polytechnique, France

[41]*University of Rochester,*
Campus Box 270171, Rochester 14627, NY, USA

[42]*CEA Paris-Saclay,*
IRFU, Batiment 141,91191, Gif-Sur-Yvette Paris, France

[43]*SINP,*
Sector 1 Block AF, Bidhan Nagar, 700 064, Kolkata, India

[44]*Tata Inst. of Fundamental Research,*
Homi Bhabha Road, 400 005, Mumbai, India

[45]*Texas Tech University,*
Lubbock 79409, TX, USA

[46]*UC Santa Barbara,*
Santa Barbara 93106, CA, USA

E-mail: Catherine.Adloff@cern.ch, Stathes.Paganis@cern.ch

ABSTRACT: CMS is designing a new high-granularity endcap calorimeter, HGCAL, to be installed later this decade. As part of this development work, a prototype system was extensively tested with beams at CERN's SPS in 2018. The electromagnetic section of the detector called CE-E prototype, consists of 14 double-sided structures, providing 28 sampling layers. Each layer carries a hexagonal module where a multi-pad large area silicon sensor is glued between the electronics PCB and a metal baseplate. The sensor pads of approximately $1\,cm^2$ are wire-bonded to the PCB and are readout by the Skiroc2-CMS ASIC. The prototype has been exposed to beams of positrons with energies ranging from 20 to 300 GeV. Based on these data, measurements of the CE-E prototype energy resolution and linearity, position resolution, resolution on the positron angle of incidence derived from the shower axis reconstruction and shower shapes are presented and compared to detailed GEANT4 simulations.

Contents

1 Introduction

The High Luminosity-LHC (HL-LHC) is expected to commence operations in 2027. The CMS Collaboration will replace the existing endcap calorimeter with a new High Granularity Calorimeter (HGCAL) [1]. This detector is a sampling calorimeter utilising hexagonal multi-pad large area silicon sensors and plastic scintillator tiles as active materials. The calorimeter endcaps (CE) include both electromagnetic (CE-E) and hadronic (CE-H) sections. The absorber layers of the CE-E section are alternating plates of lead cladded with stainless steel or copper / copper tungsten; the active layers are made of segmented silicon sensors. The CE-H section uses stainless steel as absorber and a mixture of silicon (in the regions of highest radiation) and scintillator as active material. The choice of this particular design was made in order to cope with the significantly higher radiation and the very high pile-up environment during the HL-LHC operation, compared to the present LHC conditions.

The production of the first HGCAL silicon sensor prototypes started in late 2015 following the original HGCAL design [1]. Six-inch hexagonal modules were assembled and $1\,cm^2$ silicon

pads were connected to the Skiroc2 front end chip via wirebonds through holes in the readout PCB. Skiroc2 was developed for the CALICE collaboration [2]. The 2016 beam tests have validated the HGCAL design of the CE-E section based on such novel prototype modules and have provided the first performance measurements and comparison with simulation, albeit with a limited number of layers [3].

In October 2018, a full 28-layer electromagnetic calorimeter was assembled together with a hadronic calorimeter and placed in the H2 CERN beamline [4]. The CE-E prototype, with a depth of 27 radiation lengths (X_0) and 1.4 interaction lengths (λ_I), followed closely the CE-E design for what concerns the silicon active material, the longitudinal segmentation and the choice of absorber materials. An improved version of the front-end ASIC, the Skiroc2-CMS [2], provided a large dynamic range and time over threshold information for high energy densities as well as timing information. Some differences with the design remain, like sensor size, longitudinal size, readout electronics and data acquisition (DAQ) [5]. The prototype was tested with asynchronous beams (muons, positrons and pions), with nearly no simultaneous particles and without magnetic field. An essential aim of the 2018 beam tests was to study in detail the performance of such a silicon sampling calorimeter from its response to beams of positrons with energies ranging from 20 GeV to 300 GeV.

In this paper, the performance of the CE-E prototype using positron data is reviewed in terms of energy resolution, energy linearity, spatial and angular resolutions and lateral and longitudinal shower shapes. The experimental setup is described in Section 2. The data taken and simulation production are presented in Section 3. The analysis framework is introduced in Section 4. The main results obtained with the prototype are presented in Sections 5-7, and Section 8 provides a summary and outlook.

2 Beam tests experimental setup

In this section, after introducing the beamline experimental setup, the CE-E prototype is presented with its trigger system.

2.1 CERN beamline

The data were collected during October 2018 at the H2 beam line [6], located in the EHN1 experimental hall of the CERN-SPS North Area. Secondary beams of hadrons or electrons/positrons up to a maximum momentum of 380 GeV/c or 300 GeV/c respectively are transported in the experimental areas with variable purity (10 − 99%) and rate. These secondary beams are produced by the interaction of the primary proton beam impinging on a 500 mm thick beryllium primary target, designated 'T2'. The H2 beamline transports the produced particles over a length of approximately 600 m, with the last 250 m being inside the surface EHN1 experimental hall. The H2 beamline is a magnetic spectrometer consisting of dipole magnets, quadrupoles and collimators. The beamline selects the secondary particles produced at the target within a $\Delta p/p = 0.2 − 2\%$ acceptance, depending on the collimator settings. The currents of the first and second sets of dipoles define the beam momentum emerging from the last dipole of the spectrometer located 250 m upstream of the HGCAL prototype. The uncertainty in the setting of the current in the dipole magnets corresponds to an uncertainty in the momentum of ±1 GeV. The final beam is achromatic in first order, with a fixed momentum

spread defined by the collimators. Optics-wise, only second-order chromatic aberrations introduce a negligible correlation between each particle momentum and its transverse position. For hadrons, this fixed momentum spread is the only contribution to the full momentum spread. However, for positrons, Synchrotron Radiation (SR) losses induce an additional beam momentum spread that is particularly important for energies above $100\,\text{GeV}$. In the case of positrons, SR losses in the dipole magnets also lead to a final beam momentum that is biased systematically lower than the nominal one. The beam momenta and momentum spreads are given in Table 1 for different nominal momenta.

Table 1: H2 beamline positron momenta and momentum spreads extracted from the simulation of the full beamline described in Section 3. The Gaussian fit means and standard deviations of all particle momenta at the entrance of the CE-E, were taken as the final beam momenta and momentum spreads.

Nominal Momentum [GeV/c]	Final Momentum [GeV/c]	Final Momentum Spread [GeV/c]	Final Momentum Resolution %
20	20.00	0.06	0.3
30	30.00	0.08	0.3
50	49.97	0.12	0.3
80	79.91	0.19	0.2
100	99.81	0.22	0.2
120	119.64	0.28	0.2
150	149.16	0.35	0.2
200	197.40	0.47	0.2
250	243.84	0.60	0.2
300	287.65	0.79	0.3

The H2 beamline and HGCAL prototype experimental setup is shown in Fig. 1 The beamline section from the last spectrometer dipole to the face of the calorimeter includes sections of air, beam windows and beam counters like delay wire chambers (DWC) and Cerenkov detectors accounting for about $0.5\,X_0$ of material.
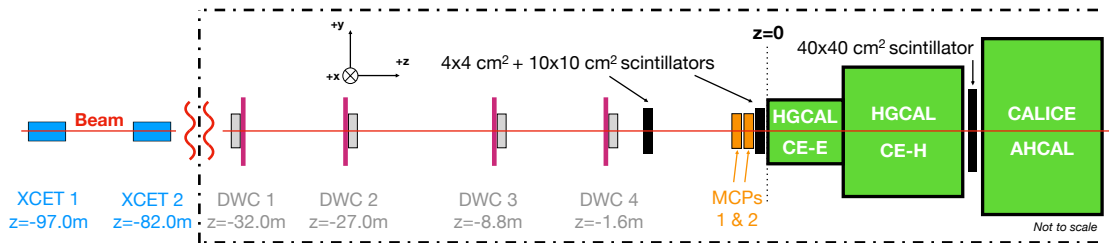
Figure 1: H2 beamline and HGCAL-prototype experimental setup.

2.2 HGCAL Prototype

The HGCAL prototype tested in October 2018 comprised a CE-E and a CE-H section. The CE-E section consisted of 28 sampling layers of hexagonal modules with hexagonal Si pads ($\approx 1.1\,\text{cm}^2$ per pad) interleaved with alternating copper and copper-tungsten absorbers or lead and stainless steel absorbers. For the 2018 beam test, 28 hexagonal modules were assembled as a glued stack of a copper-tungsten baseplate, a polyimide foil, a silicon sensor and a readout PCB (referred to as Hexaboard).

The modules followed the same basic design as the prototypes tested in 2016, albeit with better grounding to improve the electronic noise and using the new Skiroc2-CMS front-end chip [7]. The Skiroc2-CMS ASIC was specifically designed for HGCAL requirements. It offered a broad range of energy measurement thanks to a dual-gain amplification and an additional time-over-threshold technique (ToT) to cope with very high energy deposits where the low-gain channel saturates. For the low and high-gain chains, signals collected from each Si pad were amplified, shaped, sampled with a 25 ns frequency and finally stored in a 13 Switch Capacitor Array rolling analog memory (SCA). The ASIC also provided a time-of-arrival measurement (ToA) to study the feasibility of precise time measurements to contribute to pileup rejection [8]. These changes aimed to get closer to the HGCAL ultimate performance and validate the simulation on which rely all high level analyses.

The flexible nature of the prototype tested in 2018 allowed us to study a variety of three configurations, among which the two first had identical CE-E sections of 28 instrumented layers, close to the HGCAL design. The results presented in this work were based on the data taken with the first configuration, for which the CE-E layout is shown in Fig. 2. In this configuration the last cassette contains two Si sensors of 200 μm instead of 300 μm for all other sensors [4]. Table 2 gives the corresponding peak value of the simulated energy deposited by 150 GeV muons in the Si sensors, ΔE_i^{Si}. The depth, z, in radiation length before each Si sensor are given in Table 2 as well as the thickness, Δz, in radiation length between two Si sensors and the corresponding mean energy loss for a MIP, ΔE_i^{Abs}, from [9]. The silicon modules 21 to 23 were built on a copper baseplate and a 1.2 mm Cu/W plate was added in front of them, increasing therefore the mean energy loss for the absorbers 22 and 24. Further details on the CE-E and CE-H sections can be found in [4].

A complete description of the data acquisition system can be found in [5]. The acquisition of the positron data was triggered by the coincidence of two scintillators upstream of the calorimeter and the veto of a scintillator downstream the CE-H section. An event corresponds to the data recorded after a coincidence of trigger counters.

3 Data and Simulation Samples

The CE-E prototype was exposed to muon, positron and pion beams. In this publication only the exposure to positron beams is discussed, with a data set including nominal positron beam energies ranging from 20 GeV to 300 GeV. Around 100k events per positron beam energy were recorded.

An event selection, defined in Section 4.2, was used to obtain event samples with a high positron purity, with almost no shower originating upstream of the prototype and full lateral containment of the positron shower within the prototype. Between 30% and 75% of the recorded events passed the event preselection criteria depending on beam energy and beam settings. The main event loss arose from a geometric cut on the impact position of the impinging track.
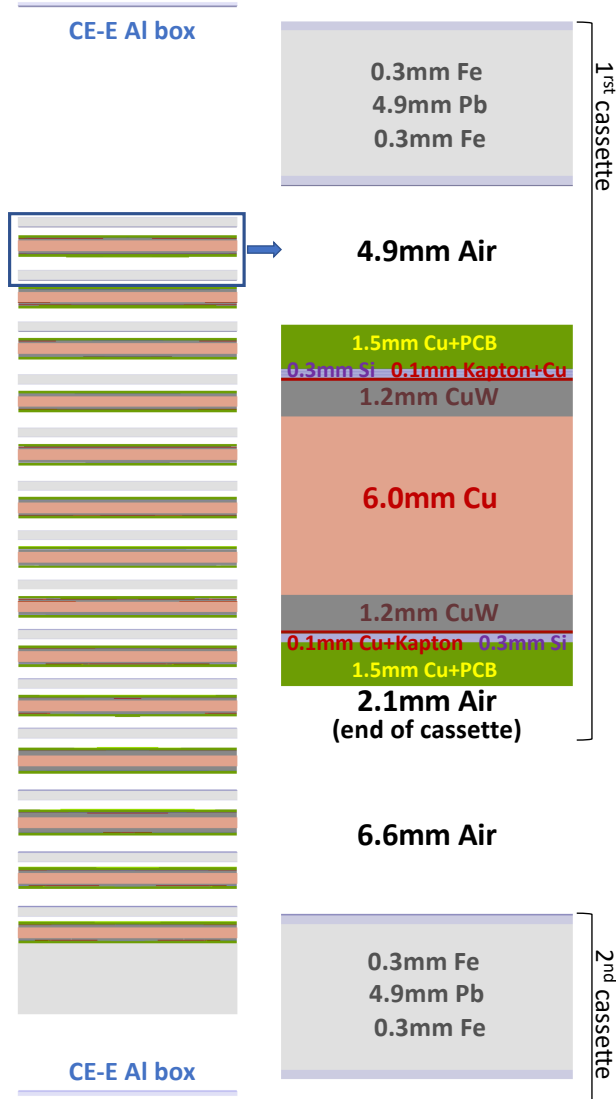
Figure 2: Layout for the CE-E prototype. This prototype was built of 14 cassettes, where each cassette carries two hexagonal modules. During the beam tests, the beam entered the prototype through the first cassette. In a hexagonal module, the Si sensor was located between the copper-tungsten plate (dark grey) and the Hexaboard (green). A cassette started with a lead plus stainless steel absorber (light blue and light grey) and ended at the Hexaboard of the second module. The cassette end was enclosed by a Mylar sheet, held by an aluminium frame (not represented here). The zoomed-in area shows the first cassette. The lead plus stainless steel absorber of the second cassette is also shown including the air gap between two cassettes. The two drawings are proportionally scaled.

The various detector setup configurations mentioned in Section 2.2 were simulated with the GEANT4 toolkit version 10.4.3, [10], using the FTFP_BERT_EMN physics list. For all results

Table 2: Relevant characteristics of the CE-E prototype. The second column gives peak value of the simulated energy deposited by 150 GeV muons in the Si sensors. The third and thourth columns give the calorimeter depth before each Si sensor and the thickness between two Si sensors in units of radiation length X_0. The fifth column gives the mean energy loss for a MIP [9] in the absorber layers. The last column gives the average of the mean energy deposited by a MIP in the absorber before and after the Si sensor except for the last layer where $\Delta E_{28}^{\text{Abs}}/2$ is given. The sum of the second and last column is for each layer the dEdx weight as given in Eq. 5.6.

Layer Number i	Energy Loss ΔE_i^{Si} [MeV]	Depth z [X_0]	Absorber Thickness Δz [X_0]	Energy Loss ΔE_i^{Abs} [MeV]	Average $(\Delta E_i^{\text{Abs}} + \Delta E_{i+1}^{\text{Abs}})/2$ [MeV]
1	$85. \ 10^{-3}$	1.00	1.00	10.2	11.29
2	$85. \ 10^{-3}$	1.98	0.98	12.3	9.85
3	$85. \ 10^{-3}$	2.92	0.94	7.4	9.85
4	$85. \ 10^{-3}$	3,90	0.98	12.3	9.85
⋮	⋮	⋮	⋮	⋮	⋮
19	$85. \ 10^{-3}$	18.23	0.94	7.4	9.85
20	$85. \ 10^{-3}$	19.21	0.98	12.3	9.85
21	$85. \ 10^{-3}$	20.15	0.94	7.4	11.36
22	$85. \ 10^{-3}$	21.30	1.15	15.4	11.36
23	$85. \ 10^{-3}$	22.23	0.94	7.4	11.36
24	$85. \ 10^{-3}$	23.38	1.15	15.4	11.36
25	$85. \ 10^{-3}$	24.31	0.94	7.4	9.85
26	$85. \ 10^{-3}$	25.29	0.98	12.3	9.85
27	$57. \ 10^{-3}$	26.23	0.94	7.4	9.85
28	$57. \ 10^{-3}$	27.21	0.98	12.3	6.17

presented here, the input of the HGCAL prototype simulation was a multiple particle gun constructed with the output of the particle tracking simulation program G4BEAMLINE based on GEANT4 [11]. The physics list used for the beamline simulation was FTFP_BERT_EMZ. The beam content at the exit of the target was set to 90% of positrons and 10% of protons. At the level of the calorimeter the proton contamination drops to zero for energy larger than 150 GeV. The empirical estimation of proton contamination does not influence the final results due to the event preselection described in Section 4.2. All known H2 beamline elements (passive and active) were included from the exit of the T2 production target to the HGCAL prototype. This consisted of numerous elements such as quadrupoles/dipoles, bending magnets, collimators, beam windows, beam pipes, scintillator counters, air sections (40% relative humidity), materials of fixed experiments NA61/SHINE and DWCs, all present along the beam trajectory. This novel simulation framework provided the best description of the beamline and therefore, within the systematics of exact initial particle production, the best description of the beam characteristics at the entrance of the prototype. For example, with the October 2018 H2 beamline setup, the G4BEAMLINE simulation generated beam position spread

at the entrance of the HCGAL prototype in agreement with the CE-E data as every particle exiting the target was propagated along the entire H2 beamline.

Data measurements of the CE-E detector relative angle with respect to the beam z axis presented in Section 6 and of the x and y beam offsets with respect to the prototype center (for each energy point) were taken into account in the beam gun parameters of the detector simulation to reproduce the position of the calorimeter with respect to the beam. The simulation of the calorimeter response is performed only if the same trigger condition as for the data is satisfied. The final number of events produced is around 100k per beam energy.

The effect of the electronics noise at the level of the measured energy in a Si pad was included in the simulation. Pad non-uniformity in response, pad-to-pad cross talk, digitization and other electronics effects were not considered. However, in the transverse shower shapes studies, a specific simulation was tested including cross talk as measured on hexagonal modules using a charge injection system.

The DWCs were not defined as sensitive material in the HCGAL simulation, hence their measurements were not produced by GEANT4. Instead, the beam trajectory was used to estimate the particle impacts in the DWCs. For the full beamline simulation, the beam trajectory was computed from the direction and position of the highest energetic charged particle at the entrance of the HGCAL. Those impact points were smeared by a Gaussian function according to the estimated DWC intrinsic resolution of 500 μm in x and y to obtain the simulated DWC measurements [12]. This results in a 430 μm precision on the extrapolated particle incidence on the CE-E prototype.

4 Analysis Framework

The analysis was based on physical quantities such as energy deposited, position and time for each Si pad, as well as track information, reconstructed from the data collected during the October 2018 beam tests. In this section, we proceed with a brief description of the reconstruction framework and a presentation of the analysis preselection.

4.1 Reconstruction Framework

The raw data from Skiroc2-CMS ASIC consisted of the digitized readout of the 13 SCA analog memories of the low and high gain channels, as well as the ToT readout and ToA readout. The pad locations in cartesian coordinates, (x_i, y_i, z_i), were retrieved from hard-coded maps of the Skiroc2-CMS ID's to their locations inside the detector, as well as from the mapping of the connected channels to the diodes on the sensors. The z axis direction was the beam direction.

The reconstruction steps to obtain the energy deposited in a Si pad in MIP units are described in detail in [4]. They are summarized below as follows:

- For each SCA memory, pedestals were determined and subtracted. After pedestal subtraction, the common mode noise in a given hexagonal module, i.e. for four ASICs, was estimated for each time sample and subtracted.

- The corrected SCA readout values were time-ordered to get the reconstructed pulses as a function of time. The obtained pulses were fitted providing the signal amplitudes of the
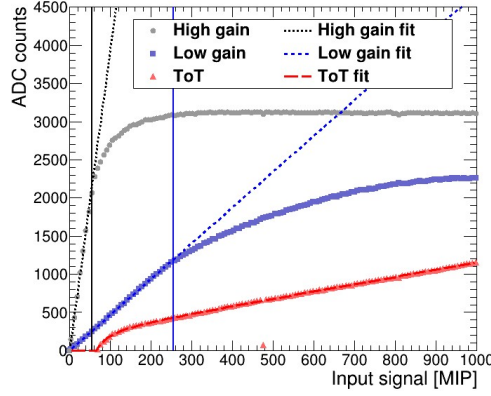
Figure 3: High-gain and low-gain amplitudes and ToT output as a function of the input charge expressed in MIP units (one MIP is approximately 3 fC). The vertical solid lines mark the maximum input signals where the high-gain and low-gain shaper outputs were linear.

low-gain and high-gain chains, A^{LG} and A^{HG}. For the ToT, the offset subtracted readout values gave directly an estimate of the signal amplitude A^{ToT}.

- Subsequently, the Si pad signal A'_{HG} was computed using the most appropriate readout value determined from the linear regions of the high and low gains and the ToT :

$$
A'_{\mathrm{HG}} = \begin{cases} A^{\mathrm{HG}} & , \text{if } A^{\mathrm{HG}} < \mathrm{HG}_{\mathrm{sat}} \\ A^{\mathrm{LG}} \cdot m_{\mathrm{HG/LG}} & , \text{if } A^{\mathrm{HG}} > \mathrm{HG}_{\mathrm{sat}} \text{ and } A^{\mathrm{LG}} < \mathrm{LG}_{\mathrm{sat}} \\ A^{\mathrm{ToT}} \cdot m_{\mathrm{LG/ToT}} \cdot m_{\mathrm{HG/LG}} & , \text{otherwise} \end{cases} \quad (4.1)
$$

where, $m_{\mathrm{LG/ToT}}$ and $m_{\mathrm{HG/LG}}$ are scale factors from LG to ToT and from HG to LG, respectively. $\mathrm{HG}_{\mathrm{sat}}$ is the threshold above which the A^{LG} was used, and $\mathrm{LG}_{\mathrm{sat}}$ is the threshold above which the A^{ToT} was used. This is illustrated in Fig. 3. Using the positron data, we determined these parameters for as many readout channels as possible. For channels away from the beam axis with low hit occupancy, the average value of the parameters for the corresponding chip or Hexaboard was used. This step is the per channel gain calibration.

- Finally, the Si pad energy $E^{\mathrm{Si}}_{\mathrm{pad}}$ in MIP units is retrieved using the following :

$$
E^{\mathrm{Si}}_{\mathrm{pad}}[\mathrm{MIP}] = A'_{\mathrm{HG}} \cdot M_{\mathrm{MIP/HG}}. \quad (4.2)
$$

The $M_{\mathrm{MIP/HG}}$ constant of each pad was obtained from the peak value, referred to as MIP value, extracted from a Landau convoluted with a Gaussian fit of the high-gain signal amplitudes distribution using muon data. Although these muons are not "minimum ionizing particles" for simplicity we refer to them as such. This last step represents the pad intercalibration.

In simulation, to allow comparison with data, the true energy deposited in a Si-pad convoluted with electronic noise was directly converted in units of the energy deposited by 150 GeV muons given by the simulation itself. Hence, the simulation uses generated energy from Si pads that are, by definition, perfectly calibrated. It should be noted that the conversion factor was extracted depending on the two different Si thicknesses of the CE-E sensors (see Section 2.2).

For both data and simulation, the upstream trajectory of beam particles was reconstructed using the available DWC measurements. For data, alignment corrections for translation offsets in x and y positions were derived through comparison of the calorimeter hit position on the first layer with the hit obtained from DWC track extrapolation.

4.2 Hit and Event Preselection

A preselection was used to obtain high positron purity and a high-quality dataset. This selection concerns both the calorimeter hit level and the event level and is applied to data and simulation. For hits, the requirements were the following.

a) Hits must have their corresponding pad energy above 0.5 MIPs. This cut was chosen to be well above the typical noise of 1/7 MIP for the high-gain chain in the CE-E section as measured in [4].

b) Hits must not come from abnormally noisy channels or from the channels of one defective chip in the first layer. 1.6% of channels are affected by this cut.

The following criteria define the event selection.

i) The presence of a single track reconstructed from measurements in all available DWCs installed just upstream of the calorimeter was required. This requirement rejects part of the events with shower starting upstream of the prototype.

ii) Events with more than 50 selected hits in the hadronic section (starting after 28 X_0) were rejected as well as events with less than 95% of the measured energy in both CE-E and CE-H contained in the electromagnetic section. This selection efficiently removes events with shower stemming from pions and protons [12]. In Figure 4a, the impact of this requirement on the measured energy in the active part of the CE-E detector is presented for positron events with a nominal energy of 120 GeV, where hadrons contamination was particularly significant (around 9% at the CE-E level from the beamline simulation).

iii) Events with a DWC extrapolated track at the entrance of the CE-E prototype falling outside a central 2×2 cm^2 acceptance window were rejected. This selection limits lateral losses in case of impact far from the prototype center, as well as the effect of different beam profile in data and MC. The acceptance window position was chosen to avoid events for which the center of the shower is too close to a specific pad with a defective amplifier standing in one of the layers with the highest energetic contribution. The effect of this acceptance cut on data, is presented in Fig. 4b for positron events with a nominal energy of 120 GeV, showing an increase of the mean of the measured energy.

The shift the energy peaks between data and MC, observed in Fig. 4a and Fig. 4b, is discussed in Section 5.

5 Energy resolution and linearity

In this section, the performance of the 2018 CE-E prototype is studied in terms of energy resolution and energy linearity. These results are obtained for the first time from a prototype with number of
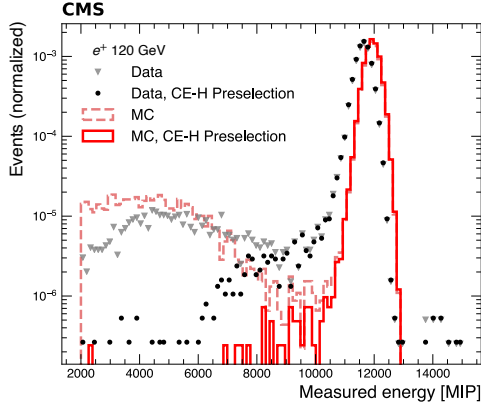
Figure 4a: Comparison of the measured energy for selected hits in the CE-E prototype before and after the selection cuts described in item ii) using the CE-H prototype information. Hadron contamination in positron beam is suppressed. The positron nominal energy is 120 GeV.
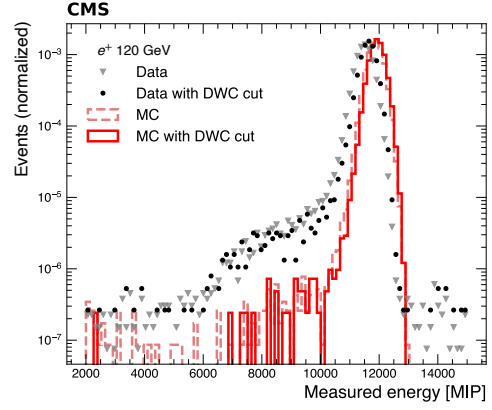
Figure 4b: For selected hits and after the CE-H preselection, comparison of the measured energy before and after the DWC acceptance cut described in item iii). The positron nominal energy is 120 GeV.

layers identical to the HCGAL design and over a wide energy range. Of particular interest is the agreement between data and MC.

After the procedure described in Section 4.1 and the hit preselection defined in Section 4.2, the unclustered measured energy in units of MIPs is taken to be the sum of the Si pad energies in the CE-E section. The measured energy distributions in data and simulation are shown in Fig. 5 for four positron energies. A factor of 1.035 is applied to the data in order to be able to better compare with the MC. For each positron energy, the data and MC distributions are fitted with a Gaussian function within the range $[\mu - 1.0\sigma, \ \mu + 2.5\sigma]$. The asymmetric interval is chosen to avoid biasing the Gaussian mean and standard deviation by the presence of a remaining low energy tail in the distributions. These tails are due to radiation losses and losses from interactions of positrons with non homogeneous material along the straight section of the beamline upstream of the calorimeter. The Gaussian fit mean μ and standard deviation σ are taken as the mean energy response $\langle E \rangle$ and resolution σ_E of the detector active part at a given beam energy. As discussed in Section 2, the estimation of the final beam energies at the entrance of the calorimeter takes into account systematic SR losses (up to 4% of the beam energy at 300 GeV). In this analysis, we have neglected the systematic errors of the estimated beam energies coming from uncertainties in the magnetic field of the dipole magnets defining the momentum and from possible missing material in the beamline simulation. In Figure 6a the measured energies in the data are compared to those in MC as a function of the beam energies, after applying a factor of 1.035 to the data points. The lower panel in Figure 6a demonstrates that the measured energies are 3.5% lower in data than in MC, independently of the positron energy at a 2% level. In Figure 6b, the energy linearity is shown. The linearity here is defined as the relative difference of the reconstructed positron energy with respect to the beam energy. To reconstruct the positron energies, the measured energies have been scaled by a slope-factor m determined from a linear fit in which the slope and intercept were allowed to float. The residuals with respect to the fitted straight line are less than 1% for data and 0.5% for MC.
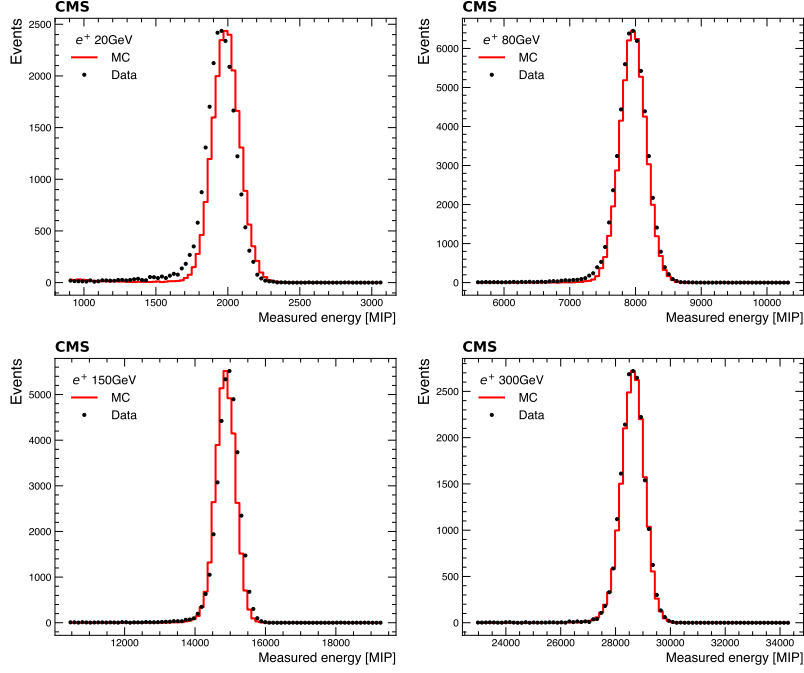
Figure 5: Measured energy distributions for data and simulation (normalized to the number of events in data) for nominal positron beam energies ranging from 20 to 300 GeV. A factor of 1.035 is applied to the data.
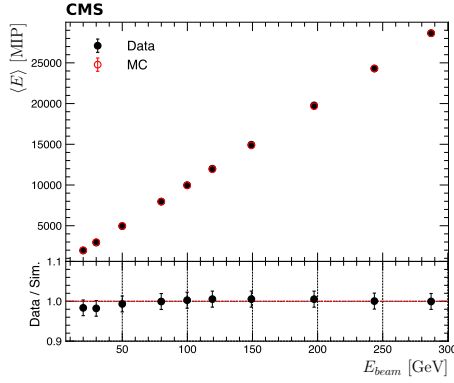
Figure 6a: Mean measured energy as a function of the beam energy for data and simulation. A factor of 1.035 is applied to the data points.
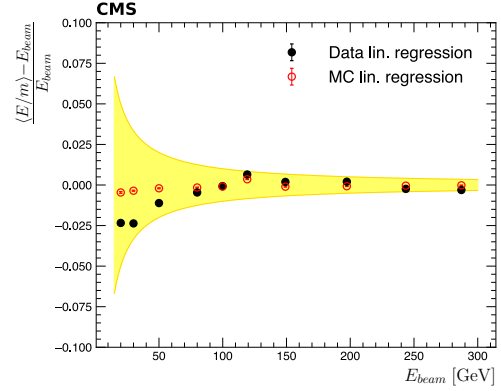
Figure 6b: Reconstructed energy linearity. The measured energies have been scaled by a slope-factor m determined from a linear fit in which the slope and intercept were allowed to float. The yellow band represents the relative error on the beam energy from the uncertainty of the dipole currents corresponding to an uncertainty of ± 1 GeV in momentum.

Figure 6b also displays the relative error on the beam energy from the uncertainty of the dipole
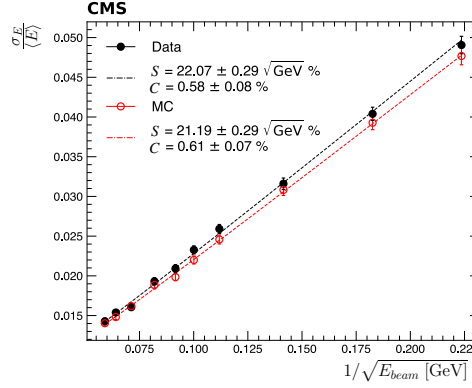
Figure 7: Measured energy resolution for data and simulation.

currents (yellow band), which is not implemented in the full beamline simulation. The linearity, without correction for losses upstream the calorimeter, is better than 3% for data and 1% for the simulation.

The measured energy resolution $\frac{\sigma_E}{\langle E \rangle}$, is shown in Fig. 7 for data and simulation . The resolution measurements are fitted as a function of E_{beam} using the function:

$$\frac{\sigma_E}{\langle E \rangle} = \frac{S}{\sqrt{E_{\text{beam}}}} \oplus C, \tag{5.1}$$

where S is the stochastic term and C the constant term. The fit function used does not include a noise term because its residual contribution was found to be negligible after the hit preselection chosen to reject noisy channels. The fitted functions are displayed in Fig. 7 and the parameter values are given in Table 3. A good agreement between data and MC for both the stochastic and constant terms is observed. The fact that the constant term in data of 0.6% is close to the one predicted by the simulation, shows that there is no significant non-uniformity of energy response within the fiducial window defined by the DWC cut.

The electromagnetic energy linearity and resolution has been studied using two alternative methods.

a) The Sampling Fraction (SF) method is based on the average sampling fraction over the complete detector [13] estimated with the GEANT4 simulation for each beam energy E_{beam}:

$$SF(E_{\text{beam}}) = \frac{\sum_{i=1}^{28} \left(E_i^{\text{Si}} \right)}{\sum_{i=1}^{28} \left(E_i^{\text{Si}} + E_i^{\text{Abs}} \right)}. \tag{5.2}$$

The reconstructed energy deposited in the complete detector is written as:

$$E = SF(E_{\text{beam}})^{-1} \times \sum_{i=1}^{28} \left(E_i^{\text{Si}} \right), \tag{5.3}$$

which consists of applying a unique weight to all layer measured energies but depending on the positron energy. The energy dependent weight only affects the linearity but does not alter the energy resolution determined from the measured energies (labelled "Meas" in Table 3).

It should be noted here that the measured energy in the silicon sensors is in MIP units so we use the conversion factor obtained from simulation (see Section 4.1) to get the measured energy in GeV.

b) In case of the dEdx method, the energy deposited in the absorber i is predicted as follows:

$$n_i^{\text{Abs}} \times \Delta E_i^{\text{Abs}}, \tag{5.4}$$

where $\Delta E_i^{\text{Abs}} = \dfrac{dE}{dx}\Big._i^{\text{Abs}}(\text{MIP mean}) \times \Delta x_i^{\text{Abs}}$ is the mean of the energy deposit for a MIP in the absorber layer i and n_i^{Abs} is the number of MIPs crossing the absorber under consideration. In this work the number of MIPs passing through the absorber layer i is taken to be the average of the number of MIPs measured in the two silicon layers located respectively before and after the absorber, $E_{i-1}^{\text{Si}}[\text{MIP}]$ and $E_i^{\text{Si}}[\text{MIP}]$. For the first absorber we assume one charged incident particle:

$$n_1^{\text{Abs}} = \frac{1 + E_1^{\text{Si}}[\text{MIP}]}{2} \text{ and}$$

$$n_i^{\text{Abs}} = \frac{E_{i-1}^{\text{Si}}[\text{MIP}] + E_i^{\text{Si}}[\text{MIP}]}{2} \text{ for } i = 2, ..., 28. \tag{5.5}$$

To count the number of MIPs in the Si sensor, $E_i^{\text{Si}}[\text{MIP}]$, one can divide the ADC readout by either the mean, the most probable value or the peak value of the MIP distribution in ADC as the latter is best described by a Landau distribution convoluted with a Gaussian function that models the noise. This choice is only changing the total calorimeter energy scale, so we use the better experimentally determined peak value to perform the pad intercalibration. The combination of equations 5.4 and 5.5 results in an estimate of the total energy E deposited in the passive and active layers of the prototype :

$$E = \frac{\Delta E_1^{\text{Abs}}}{2} + \sum_{i=1}^{27} \left(\frac{\Delta E_i^{\text{Abs}} + \Delta E_{i+1}^{\text{Abs}}}{2} + \Delta E_i^{\text{Si}} \right) \times E_i^{\text{Si}}[\text{MIP}] + \left(\frac{\Delta E_{28}^{\text{Abs}}}{2} + \Delta E_{28}^{\text{Si}} \right) \times E_{28}^{\text{Si}}[\text{MIP}]$$

$$= \frac{\Delta E_1^{\text{Abs}}}{2} + \sum_{i=1}^{28} \left(W_i \, E_i^{\text{Si}}[\text{MIP}] \right), \tag{5.6}$$

where $\Delta E_i^{\text{Si}} = \dfrac{dE}{dx}\Big._i^{\text{Si}}(\text{MIP peak}) \times \Delta x_i^{\text{Si}}$ is the peak value of the simulated energy loss distribution for a MIP in the Si sensor i, namely the factor used in simulation to convert the Si sensor energy into MIP units as discussed in Section 4.1. The ΔE_i^{Abs} values are computed using the PDG [9] mean energy losses per traverse thickness for the absorber materials. The dEdx weights, W_i, are independent of the beam energy but depend on the layers.

For the SF method applied to the tested calorimeter [14], there is less than 0.4% difference between the sampling fraction at 30 GeV and at 300 GeV, so this method gives almost the same performance as determined with the measured energy in terms of energy linearity. In particular, the linearity for the data does not show any improvement. For the dEdx method, the weights in equation 5.6 computed with Table 2 are identical except for the first and last layers and for four

Positron Energy Resolution						
	Meas S $[\sqrt{\text{GeV}}]$ %	Meas C %	SF S $[\sqrt{\text{GeV}}]$ %	SF C %	dEdx S $[\sqrt{\text{GeV}}]$ %	dEdx C %
Data	22.1 ± 0.3	0.58 ± 0.08	22.1 ± 0.3	0.58 ± 0.08	22.0 ± 0.3	0.53 ± 0.09
MC	21.2 ± 0.3	0.61 ± 0.07	21.2 ± 0.3	0.61 ± 0.07	21.3 ± 0.3	0.55 ± 0.07

Table 3: Positron energy resolution stochastic and constant terms for measured energies in Si, SF calibrated energies and dEdx calibrated energies for data and simulation. A good agreement between data and MC in the stochastic and constant term is observed.

layers close to the end of the CE-E prototype, due to two layers with different base plates. Therefore the dEdx is almost equivalent to the SF method that uses a single constant weight for all layers. The results in terms of energy resolution for the two methods are summarized in Table 3, showing a good agreement between data and MC. As expected the SF method provides the same energy resolutions as the resolutions obtained from the measured energies (see Fig. 7).

6 Position and Angular resolutions

In this section, the shower position and angular measurements are presented. First, two-dimensional shower impact positions are computed for each sensitive layer and position resolutions are deduced. In Section 6.1, we describe the procedure and present the results. Then, taking advantage of having a fully-equipped detector in 2018, the measurements from all 28 layers are combined in a second step to reconstruct the axis of the shower. The method and the performance of the shower axis reconstruction are discussed in Section 6.2.

In both sections, the incident particle trajectory used as a truth reference is extracted from the DWC reconstructed track. In simulation, the DWC reconstructed track is obtained from a straight-line backward extrapolation using the direction of the highest energetic charged particle at the entrance of the CE-E and smeared according to the DWC resolution (see Section 3).

6.1 Position Reconstruction for each Layer

The reconstruction of the shower impact position on each calorimeter layer follows the procedure reported in [3] which uses a logarithmic energy-weighted method:

$$x_{\text{reco}} = \frac{\sum_{i \in M} \omega\left(E_i^{\text{Si}}\right) \cdot x_i}{\sum_{i \in M} \omega\left(E_i^{\text{Si}}\right)}, \quad \text{analogous for } y_{\text{reco}}, \tag{6.1}$$

where the set M includes all selected hits within the second ring of pads around the pad with the maximum deposited energy (a total of 19 pads). The energy weighting function $\omega\left(E_i^{\text{Si}}\right)$ obtained

in [3] and used here is given by:

$$\omega(E_i^{\mathrm{Si}}) = \max\left[0,\; a + \ln\left(\frac{E_i^{\mathrm{Si}}}{\sum\limits_{j\in M} E_j^{\mathrm{Si}}}\right)\right],\quad a = 3.5\;.\tag{6.2}$$

The position residuals are defined as the reconstructed shower position minus the expected one determined from the DWC track extrapolation, $x_{\mathrm{reco}} - x_{\mathrm{track}}$ and $y_{\mathrm{reco}} - y_{\mathrm{track}}$. For each layer and positron energy, the x and y position residual distributions are fitted with a Gaussian function in the range of -2.0σ to $+2.0\sigma$ around the mean to extract the mean $\mu_{x,y}$ and the standard deviation $\sigma_{x,y}$.
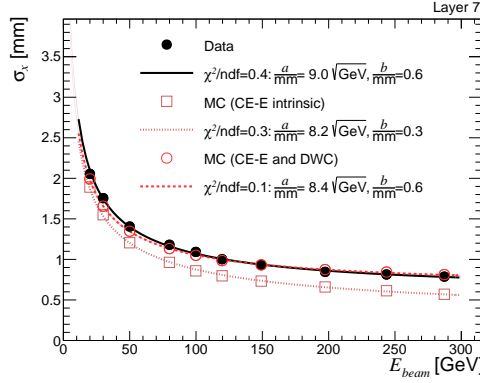
Figure 8: Combined CE-E prototype and DWC position resolution in x in one layer at a depth of 6.7 X_0 as a function of the incident positron energy for data and simulations without (CE-E intrinsic) and with DWC resolution.

The standard deviation serves as a proxy for the position resolution which is the combination of the CE-E prototype and the DWC resolutions. For data and simulation, the position resolution in x as a function of the beam energy in one layer (Layer 7), is shown in Fig 8. For simulation, the calorimeter intrinsic position resolution using the true the track position without including the DWC resolution is also shown. The position resolution may be parameterized as a function of E_{beam} using the function:

$$\sigma_x = \frac{a}{\sqrt{E_{\mathrm{beam}}}} \oplus b,\;\text{ analogous for } y,\tag{6.3}$$

where the stochastic term a is motivated by the sampling fluctuations in the contributing Si pads. Data and MC are fitted with this parameterization as it provides the best fit quality. At low energy, where multiple Coulomb scattering (MCS) is not negligible, a small difference between data and simulation including finite DWC resolution is observed and probably due to the straight-line extrapolation used in the simulation of the DWC measurements (see Section 3). For positron energies greater than 100 GeV, the simulation including finite DWC resolution reproduces well the data position resolution and the quadratic difference between the two simulations agrees with the DWC tracking resolution. This confirms a good modelling of the DWC measurements in the simulation. In this energy range, the intrinsic position resolution from the simulation, better than

0.8 mm, gives a good estimation of the intrinsic resolution which can be obtained with the tested device close to the electromagnetic shower maximum. With a better tracking and a full beamline simulation, the layer position resolution reproduces the findings from the 2016 beam tests [3].

## 6.2 Reconstruction of the Shower Axis

To obtain the best estimation of the shower position and angle resolution, the individual layers are first aligned [14]. The shower axis is determined from a straight line fit to per-layer shower positions for layers in which 1% to 95% of the total shower energy is deposited.

In this section, the pointing residual is defined as the difference between the reconstructed shower axis impact evaluated at the depth equal to the shower longitudinal center of gravity and the expected impact determined from the DWC track extrapolation. The shower longitudinal center of gravity, COG_z in radiation length units, is defined as:

$$COG_z[X_0] = \frac{\sum_{i=1}^{28} E_i^{\text{Si}} \cdot z_i[X_0]}{\sum_{i=1}^{28} E_i^{\text{Si}}}, \tag{6.4}$$

where E_i^{Si} is the Si deposited energy in the layer i and $z_i[X_0]$ the total radiation length up to Si layer i. The linear fits of the pointing residual means as a function of ΔCOG_z are used to estimate the relative angles in x and y between the CE-E prototype and the DWCs [14] . ΔCOG_z represents the difference of the shower COG_z with respect to its average in the given dataset. The resulting fit angles are around 10 mrad with an error less than 0.8 mrad. These relative angles were included in the simulation as the angles between the calorimeter and the beam.

After layer alignment, the combined shower axis and DWC pointing resolution in x at $z = COG_z$ is shown in Fig. 9a. The parameterization defined Eq. 6.3 is used to fit this resolution and describes the data reasonably well. At high energy, the axis position resolution reveals a small difference between data and MC. This is probably due to minor mis-modeling of the DWC measurements as the DWC resolution used in the simulation was extracted from 200 GeV muon data (see Section 3). At the highest tested energies, the estimated intrinsic position resolution of the calorimeter is found to be better than 0.3 mm.
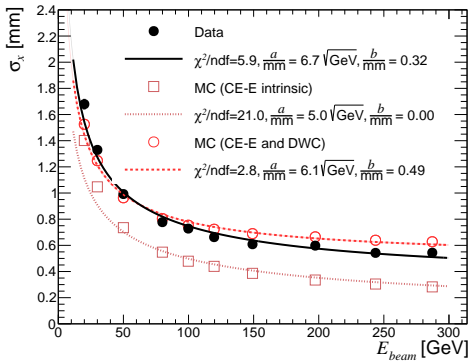
Figure 9a: Combined shower axis and DWC pointing resolution at $z = COG_z$ for data and simulations without (CE-E intrinsic) and with DWC resolution.
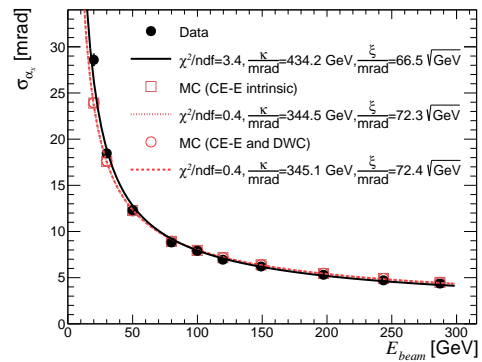
Figure 9b: Shower axis angular resolution for data and simulations without (CE-E intrinsic) and with DWC resolution.

The reconstructed shower axis angular resolutions in x and y are determined and σ_{α_x} as a function of the beam energy is shown in Fig. 9b. The following empirical parameterization with noise- and stochastic-like constants κ and ξ renders the best description of the angular resolution dependence on the beam energy:

$$\sigma_{\alpha_x} = \frac{\kappa}{E_{\text{beam}}} \oplus \frac{\xi}{\sqrt{E_{\text{beam}}}}, \quad \text{analogous for } y. \tag{6.5}$$

Data and simulation are in excellent agreement for energies larger than 30 GeV. Note that due to the large spacing between the DWCs in the setup, the effect of the intrinsic DWC resolution on the reconstructed track angle is negligible, as this is evident from the overlap of the curves representing the two simulations. For data and simulation, the angular resolution at the highest energy point is below 5 mrad.

7 Shower shape measurements

In this section, longitudinal and lateral shower-shape variables are presented and compared to simulation over a wide range of energies. The 28-layer CE-E prototype allows for fine sampling of the longitudinal profile and comparison with an empirical parameterization. The impact of crosstalk on the lateral shower shapes is also discussed.
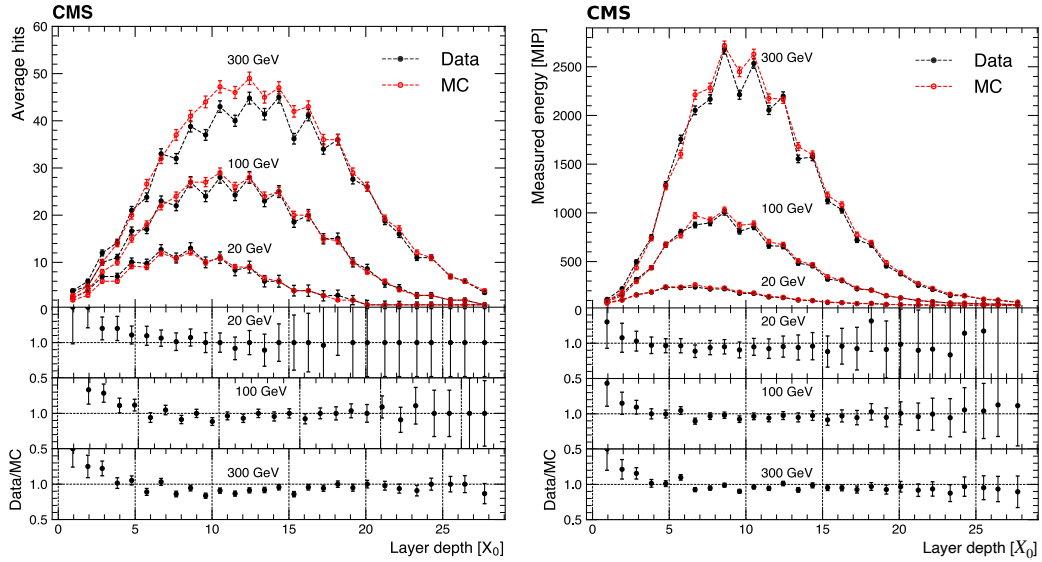
7.1 Longitudinal shower shapes

A comparison of the shower longitudinal center of gravity distributions between data and simulation is shown in Fig. 10, for nominal positron energies in the range 20 to 300 GeV. A reasonable agreement between data and simulation is observed for the full energy range. The differences observed in the rising part of the distributions can be attributed to the incomplete modeling of the H2 beam line in the simulation.

In Fig. 11, the longitudinal profiles given by the average number of hits and the median measured energy as a function of the layer depth are shown for positron nominal beam energies of 20, 100 and 300 GeV. We observe an overall agreement with the simulation over the entire detector for the two types of profiles. With the exception of the first layers, there is less energy measured in data than in MC resulting in about 3.5% less energy measured in the complete detector in data compared to MC as outlined in Section 5. The average number of hits displays also less hits for data than MC in the middle layers. Despite the fact that, for the absorbers, the mean energy loss of a MIP in even layers is close to twice the energy loss in odd layers, the measured energy of the shower is higher in odd layers than in even layers. This effect was studied in simulated showers and attributed to two causes [14]. The larger energy deposited in odd Si sensors is due to larger numbers of soft electrons, dominated by delta rays produced in the material (especially the PCB) just in front of the sensors, and larger backward-moving soft electromagnetic component by reason of the CuW plate right after the odd sensors when compare with the even layers which are followed by PCB.
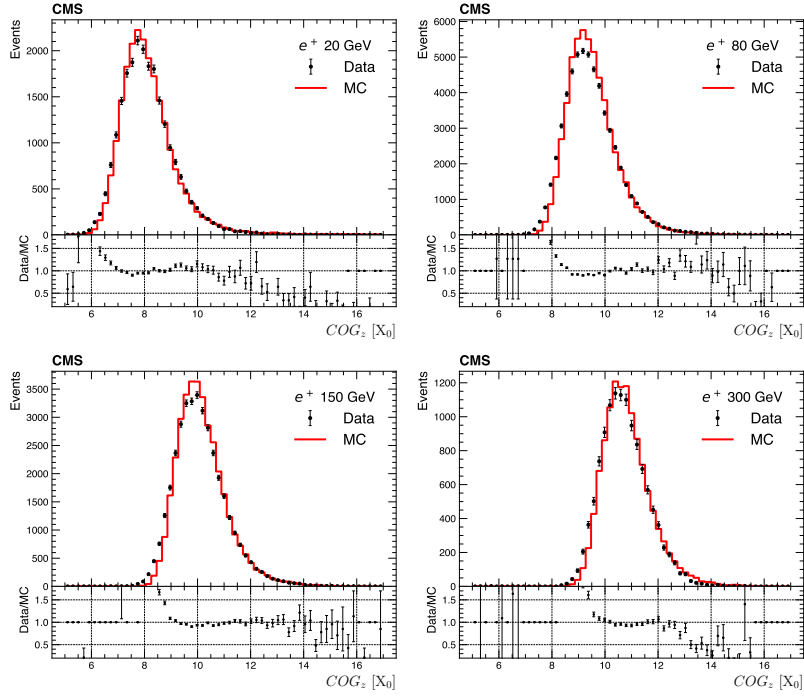
Figure 10: Distributions of shower longitudinal center of gravity (COG_z) for positron nominal beam energies ranging from 20 to 300 GeV. The simulation is normalized to the number of events in data.

Figure 11: Longitudinal shower profiles for different nominal positron beam energies given by the average number of hits (left) and the median measured energy (right).

The average longitudinal electromagnetic shower profile for homogeneous media can be described empirically using Longo's parameterization [15]:

$$\left\langle \frac{dE(t)}{dt} \right\rangle = E_0 \frac{(\beta t)^{\alpha-1} \beta \exp(-\beta t)}{\Gamma(\alpha)}, \tag{7.1}$$

where t is the depth in radiation length, E_0 is the mean of the total energy deposited in the calorimeter and α and β are the shape and scaling parameters, respectively. The analytical expression in Eq. 7.1 gives a good first-order approximation for sampling calorimeters. We fit the measured energy longitudinal profiles (including the observed longitudinal oscillations) with Eq. 7.1 to examine the expected logarithmic energy dependence of the position of the longitudinal shower maximum T given by $\frac{\alpha-1}{\beta}$. Figure 12 gives the shower maximum as a function of the beam energy. It is fitted using the following parameterization [9]:

$$T = \log(y) - 0.5, \tag{7.2}$$

where $y = E/E_c$ and E_c is the critical energy of the calorimeter. The critical energy represents the electron or positron energy for which the ionisation and excitation losses are equal to those from radiative processes (bremsstrahlung and pair creation). In all cases we obtain fit residuals at the level of 4 to 5% with no dependence on beam energy which demonstrates the validity of the $\log(y)$-dependence of T. The χ^2/ndf values are different from 1 due to the conservative estimation of the uncertainties. The obtained critical energy is 26.1 ± 4.0 MeV for data and 22.3 ± 2.8 MeV for the simulation. Detailed studies are found in [14] where the validity of the Longo's parameterization is tested using the average COG_z, either extracted from the longitudinal fit or from the event distribution.
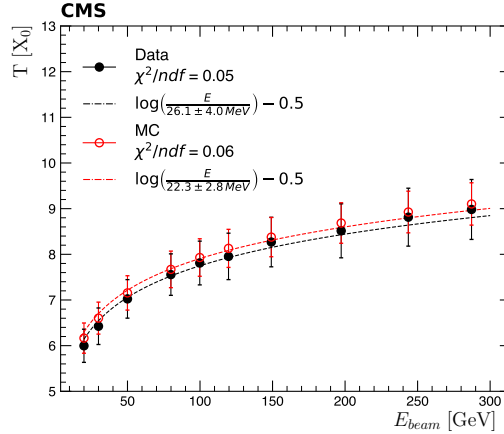

Figure 12: Shower maximum as a function of the beam energy. The shower maximum is determined from the longitudinal profile fit (error bars are evaluated by propagating the parameter fit uncertainties).

7.2 Transverse shower shapes

To study the lateral spread of electromagnetic showers in the CE-E, we first define the "seed" pad of the energy spatial distribution in each layer, the one with the maximum energy in the layer under

consideration. The transverse shower profile of a layer is given by the energy deposited in a ring of pads per units of active area as a function of its radial distance r from the seed pad, normalized to the energy of the seed pad. This representation allows, in principle, the parameterization of the lateral energy deposition as a function of shower depth and beam energy. In Fig. 13, the comparison of transverse shower profiles between data and simulation is shown for 300 GeV positrons. As expected, the energy density is steeper in the first layers. A reasonable agreement between data and simulation is observed, particularly for the most energetic pads (those nearest to the seed pad).
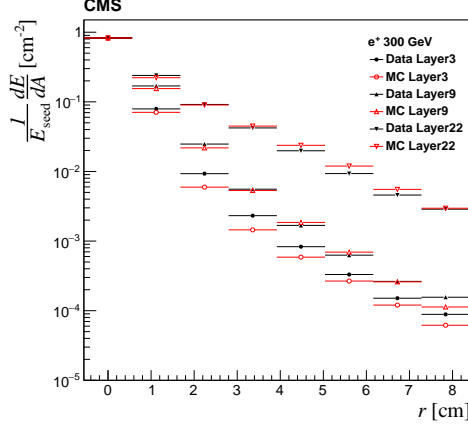
Figure 13: Transverse shower profile comparison between data and simulation for positron nominal energy of 300 GeV in layers 3, 9 and to 22. The shapes shown are the energy deposited in a ring of pads per units of active area as a function of its radial distance r from the seed pad, normalized to the energy of the seed pad in the layer under consideration.

Another method to study the transverse shower development is to calculate, for each layer, the ratios between the energy deposited in the seed pad and in the 7 pads around the seed pad, $E_{\text{seed}}/E_{7\text{pads}}$, or the ratios between the energy deposited in 7 pads and in 19 pads, $E_{7\text{pads}}/E_{19\text{pads}}$. Figure 14 shows these distributions in layers 8, 9 and 10 for positron nominal energy of 100 GeV. The $E_{\text{seed}}/E_{7\text{pads}}$ distributions appear to be slightly shifted toward higher values in data compared to simulation, whereas $E_{7\text{pads}}/E_{19\text{pads}}$ distributions display a small odd/even layer dependent shift. Potential explanations for the $E_{\text{seed}}/E_{7\text{pads}}$ difference might come from mismodeling of upstream material, beam profile, hadrons or double-cluster contaminations in the full beamline simulation not corresponding to data, missing pad-to-pad response variations and missing crosstalk effects between pads in simulation. In MC, selecting the core or one edge of the beam profile has an impact on the lateral shapes in the first layers. After application of the DWC cut described in Section 4.2, the spacial positron track impact distribution on the calorimeter is identical for data and simulation. The effect of the different beamline profile in data and simulation on the lateral shapes, is reduced by this cut. Extensive comparison between data and MC (energy resolution and linearity as well as the longitudinal shower shape) showed no significant discrepancy except of a deficit in the upstream material budget. The influence of crosstalk on the lateral shapes is studied with a dedicated simulation. The crosstalk is estimated using a charge injection system that delivers
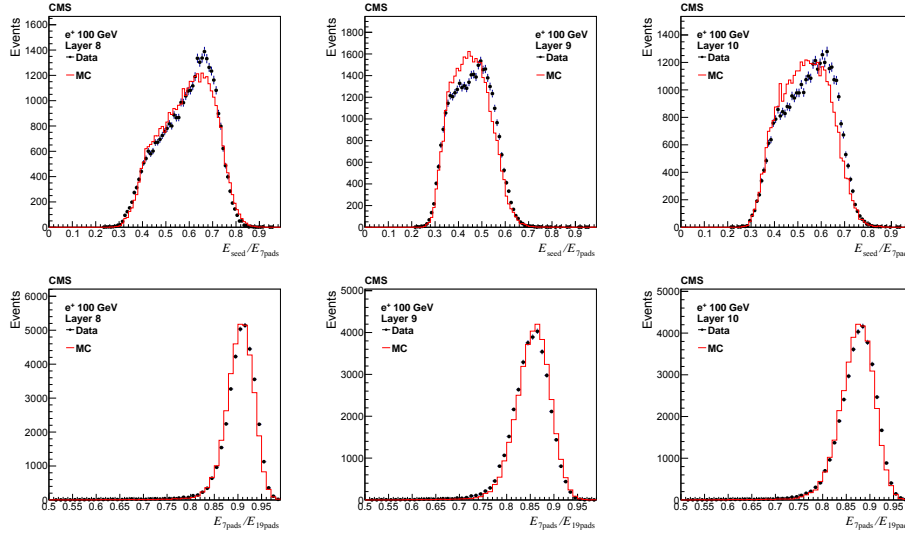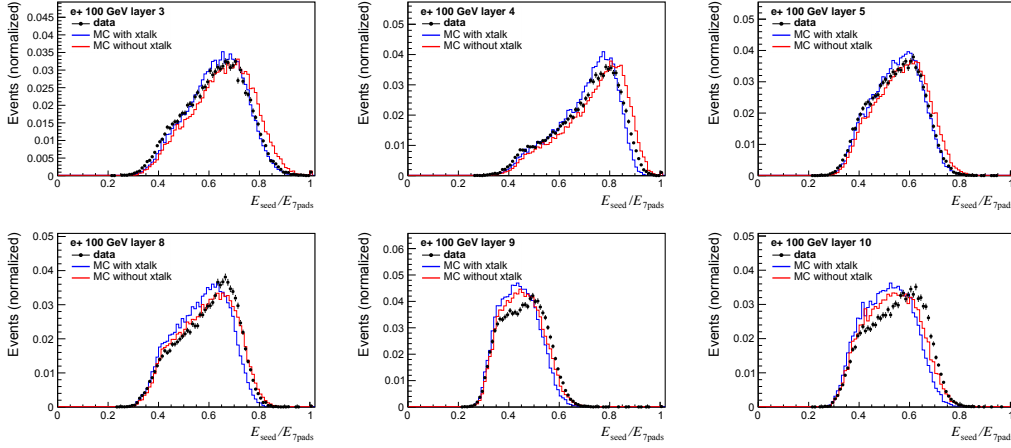
Figure 14: Distributions of $E_{\text{seed}}/E_{7\text{pads}}$ and $E_{7\text{pads}}/E_{19\text{pads}}$ for layers 8, 9 and 10 and for positron nominal beam energy of 100 GeV. The simulation is normalized to the number of events in data.

pulses to the hexaboard. Every pad induces a charge in the surrounding 6-pad ring of about 5% of the injected charge. This fraction increases very slowly with the injected charge and varies very little from pad to pad. In Fig. 15 the comparison between data and simulation, including or not in simulation this measured crosstalk, is shown in terms of $E_{\text{seed}}/E_{7\text{pads}}$ for different layers (the impact of crosstalk on $E_{7\text{pads}}/E_{19\text{pads}}$ was found to be negligible). Inclusion of crosstalk in the simulation leads to a better agreement with the data in layers up to layer 5 to 10 depending on the positron energy. This improvement was observed independently of the DWC fiducial cuts. Odd layers with more energy and larger transverse shower shape are less sensitive to crosstalk. Similarly, the impact of the crosstalk is smaller for layers around the shower maximum. In conclusion, even few-percent crosstalk effects can lead to significant distortions of the lateral shapes.

In the high pileup environment of the HL-LHC, within which the HGCAL will have to operate, the showers of single electrons or photons will have to be reconstructed against a uniformly-spread background from pileup. Therefore, a small transverse size for electromagnetic showers is desirable for good energy measurement and two-shower separation, particularly at high pseudorapidities. We define the radial containment of the energy deposition, R, by the radius of a cylinder aligned along the shower axis that contain on average 90% of the energy deposited in the shower. In the case of a homogeneous calorimeter, this quantity represents the Molière radius. The energy deposited in a cylinder of radius r aligned along the shower axis is evaluated by the quantity $E(r)$ in discrete steps of r:

$$E(r) = \sum_{i=1}^{28} E_i^{\text{Si}}(r),$$ (7.3)

where $E_i^{\text{Si}}(r)$ is the sum for the ith layer of the energy deposited in Si pads inside a given ring of pads centered on the shower axis. The corresponding discrete steps of r are such that the area of the disc of radius r corresponds to the total area of the pads used to compute $E_i^{\text{Si}}(r)$. Here the shower

Figure 15: Distributions of $E_{\text{seed}}/E_{7\text{pads}}$ for positron nominal energy of 100 GeV for layers 3 to 5 and 8 to 10. Application of the measured crosstalk in the simulation improves the agreement with the data up to layer 5.

axis is the per-event track trajectory evaluated from the DWCs. Figure 16 shows, for two positron energies, the statistical mean of $E(r)/E$ over all events, where E is the total measured energy of the calorimeter. It can be seen that 90% of the energy is contained in a cylinder of radius equal to about 3 cm, which corresponds to the central pad surrounded by two rings of 1.1 cm^2 pads. In order to obtain $\langle E(r)/E \rangle$ for all values of r, we parameterize this quantity with the following function:

$$\langle E(r)/E \rangle = 1 - A \cdot \exp(-B \cdot r), \tag{7.4}$$

where A and B are free parameters. Having obtained A and B from the fit of $\langle E(r)/E \rangle$ as a function of r, the value of R is obtained by solving $\langle E(R)/E \rangle = 0.9$. The first points in Fig. 16 are not included in the fits as the variation in the deposited energy in the central cell is a strong function of the impact point. The contribution to the error on R from the choice for the discrete r values is quite larger than the one from the fit uncertainties. For positron energies larger than 50 GeV, a good agreement between data and MC is observed. For energies between 20 GeV and 50 GeV, the increasing value of R with decreasing positron energies for both data and simulation is mainly due to the increase of scattering in the beamline upstream the calorimeter. In the same energy range, simulation predicts smaller R which could be explained by the incomplete description of the beamline in the simulation resulting in less upstream scattering. At high energy the radial containment is slightly higher than the computed Molière radius of the HGCAL design [1]. The largest contribution to the transverse spread of the electromagnetic showers in a sampling calorimeter comes from air gaps. As the air gaps in the final HGCAL are different (smaller) compared to this prototype, the importance of what is presented lies in the comparison with MC simulation.

8 Conclusion and Outlook

The performance of a 28-layer electromagnetic HGCAL prototype was studied in a CERN beam test. The detector was exposed to positron beams of nominal energies ranging from 20 to 300 GeV.
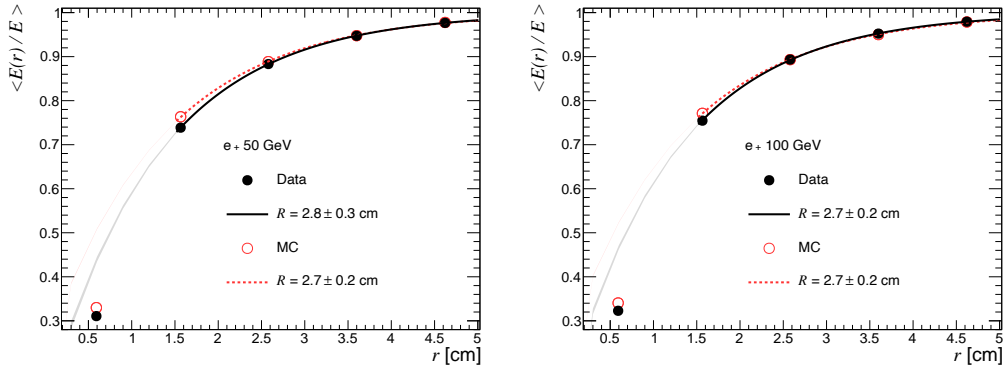
Figure 16: Statistical mean of $E(r)/E$ as a function of r for nominal positron energy of 50 GeV and 100 GeV in data and simulation. The radial containment R is extracted from the fitted exponential function defined in Eq. 7.4 using $\langle E(R)/E \rangle = 0.9$ (the error on R is evaluated by propagating the parameter fit uncertainties and by considering different choices of discrete r).

Raw data were read out for each single pad in the form of calorimeter hits, and subsequently calibrated and converted to the energy deposited in the pads in units of MIPs.

Direct comparison between data and MC in terms of measured energy showed that the data undershoots the MC by 3.5%, independent of the beam energy. Correcting for this overall scale, the agreement between data and MC in terms of absolute visible energy was found to be at the level of 2% for the full energy range. The measured energies resolution yielded a stochastic term of 22 $\sqrt{\text{GeV}}$% and constant term of 0.6%, in agreement with the simulation. The energy response linearity of the prototype was better than 2.5% using a linear fit of the measured energy. Similar performance was obtained using the reconstructed energy deposited in the CE-E prototype either with the Sampling Fraction or dEdx method.

The capabilities of the prototype were also studied in terms of the spatial and angular resolution. At the highest energy, using the reconstructed shower axis, the position resolution is less than 0.3 mm and the angular resolution is better than 5 mrad.

Lateral and longitudinal shower shapes were also measured and compared to the simulation. A good agreement was found in the case of longitudinal shower shapes for all energies. A study of the measured shapes and their comparison with the Longo parameterization was presented, showing a good agreement of measurements with this empirical analytical expression. The lateral shower shapes showed sensitivity to pad-to-pad cross talk and better agreement with MC was observed only after the measured cross talk noise was properly simulated.

Based on these results, we conclude that the full 28-layer Si prototype calorimeter exhibits a nominal performance meeting the design requirements. Although this prototype is not identical to the final design for HGCAL at HL-LHC, its excellent performance and smooth operation during the 2018 test beam at CERN, indicate that the design is sound and the detector will meet the physics requirements.

Acknowledgments

References

[1] CMS Collaboration. *The Phase-2 Upgrade of the CMS Endcap Calorimeter*. Technical Report CERN-LHCC-2017-023, CMS-TDR-019, CERN, 2017. URL https://cds.cern.ch/record/2293646.

[2] S. Callier, F. Dulucq, C. de La Taille, G. Martin-Chassard, and N. Seguin-Moreau. *SKIROC2, front end chip designed to readout the Electromagnetic CALorimeter at the ILC*. *JINST*, 6:C12040, 2011. doi:10.1088/1748-0221/6/12/C12040.

[3] N. Akchurin et al. *First beam tests of prototype silicon modules for the CMS High Granularity Endcap Calorimeter*. *JINST*, 13:P10023, 2018. doi:10.1088/1748-0221/13/10/P10023.

[4] B. Acar et al. *Construction and commissioning of CMS CE prototype silicon modules*. *JINST*, 16: T04002, 2021. doi:10.1088/1748-0221/16/04/t04002.

[5] B. Acar et al. *The DAQ system of the 12,000 Channel CMS High Granularity Calorimeter Prototype*. *JINST*, 16:T04001, 2021. doi:10.1088/1748-0221/16/04/T04001.

[6] N. Charitonidis and B. Rae. *H2 beam line*, 2017. URL http://sba.web.cern.ch/sba/BeamsAndAreas/h2/H2manual.html.

[7] J. Borg, S. Callier, D. Coko, F. Dulucq, C. de La Taille, L. Raux, T. Sculac, and D. Thienpont. *SKIROC2_CMS an ASIC for testing CMS HGCAL*. *JINST*, 12:C02019, 2017. doi:10.1088/1748-0221/12/02/C02019.

[8] D. Barney. *Timing performance of prototype silicon-sensor modules for the HGCAL in high-energy positron and pion beams at CERN*. *to be published in JINST*, 2021.

[9] M. Tanabashi et al. *Review of Particle Physics*. *Phys. Rev. D*, 98:030001, Aug 2018. doi:10.1103/PhysRevD.98.030001.

[10] S. Agostinelli et al. *GEANT4: A Simulation toolkit*. *Nucl. Instrum. Meth.*, A506:250–303, 2003. doi:10.1016/S0168-9002(03)01368-8.

[11] T. J. Roberts, K. B. Beard, S. Ahmed, D. Huang, and D. M. Kaplan. *G4BEAMLINE Particle Tracking in Matter Dominated Beam Lines*. *Conf. Proc. C*, 110328:373–375, 2011. URL https://accelconf.web.cern.ch/PAC2011/papers/mop152.pdf.

[12] T. Quast. *Qualification, Performance Validation and Fast Generative Modeling of Beam Test Calorimeter Prototypes For the CMS Calorimeter Endcap Upgrade*. *RWTH Aachen University, Aachen Germany*, 2020. doi:10.18154/RWTH-2020-06473.

[13] S. Paganis, A. Psallidas, and A. Steen. *Optimizing the Performance of a High-Granularity Silicon-Pad EM Calorimeter. JINST*, 12(06):P06013, 2017. doi:10.1088/1748-0221/12/06/P06013.

[14] N. Akchurin et al. *Detailed results of the response of a CMS HGCAL silicon-pad electromagnetic calorimeter prototype to 20-300 GeV positrons.* Technical Report CMS-NOTE-2021-009, CERN, 2021. URL https://cds.cern.ch/record/xxx.

[15] E. Longo and I. Sestili. *Monte Carlo Calculation of Photon Initiated Electromagnetic Showers in Lead Glass. Nucl. Instrum. Meth.*, 128:283, 1975. doi:10.1016/0029-554X(75)90679-5. [Erratum: Nucl. Instrum. Meth.135,587(1976)].